Materials Science & Engineering A 739 (2019) 348–356

Contents lists available at ScienceDirect

Materials Science & Engineering A

journal homepage: www.elsevier.com/locate/msea

Microscopic investigation of damage mechanisms and anisotropic evolution of damage in DP600

E.E. Aşık*, E.S. Perdahcıoğlu, A.H. van den Boogaard

Chair of Nonlinear Solid Mechanics, Faculty of Engineering, University of Twente, Enschede, The Netherlands

ARTICLE INFO

Keywords:
Steel
DP600
Damage evolution
Damage anisotropy
Damage mechanisms
Micro analysis
Interrupted tensile test

ABSTRACT

Weight reduction and fuel consumption play an important role on material selection in automotive industry. In this respect, ferritic-martensitic dual phase steels are gaining popularity thanks to their versatile combination of strength and formability. In this study, we investigate evolution of damage and active damage mechanisms in a commercial DP600 steel. Interrupted tensile tests are conducted in both rolling (RD) and transverse directions (TD). Subsequently, damage mechanisms and void evolution is characterized by cross-sectional SEM micrographs. The results reveal that, in both RD and TD, damage occurs by three different damage mechanisms. Namely, void formation due to inclusions, cracking of martensite islands and decohesion between ferrite and martensite. From these damage mechanisms, void formation due to large inclusions occur in the early stages of deformation, whereas the other two are both active throughout the complete stretching. The most commonly observed damage mechanism was martensite cracks and seem to be the primary reason of failure. In addition, void evolution studies clearly show that damaged area as well as number of voids increase more rapidly in RD than TD. Furthermore, in both directions, damage concentrates at the mid plane of the specimens, leading to an inhomogeneous distribution of voids in the thickness direction.

1. Introduction

Environmental issues and sustainability concerns are pushing all industries to produce greener and more sustainable products. In structural applications, these concerns show themselves in producing lighter but still stronger materials. Automotive industry, for example, demands new types of steel grades, which have higher strength, better formability and high toughness. Consequently, total mass reduction as well as lower energy consumption during metal forming would be achieved without sacrificing from strength and crash-worthiness, and yield in more environmentally friendly vehicles. In this perspective, advanced high strength steels play a crucial role in structural applications due to their combination of versatile mechanical properties such as high strength to weight ratio, high tensile strength to yield ratio and excellent formability. Furthermore, dual phase (DP) steels with the relative ease of controlling mechanical properties in predefined ranges, proved themselves as promising candidates which satisfy the needs of the automotive industry [1–3].

Dual phase steels are named after their two main constituent phases; ferrite and martensite. In addition, DP steels may contain some amount of bainite or retained austenite. Depending on the production parameters, martensite fraction and morphology can be controlled to obtain a specific grade of DP steel. The classification of this steel grade is done according to their ultimate tensile strength. As a general principle, in DP steels soft ferrite matrix surrounds hard martensite islands. Ferrite gives ductility to the alloy whereas martensite ensures the necessary strength. The combination of two mechanically diverse phases in such a complex microstructure gives the versatile properties of DP steels [4–7]. Nevertheless, damage initiation mechanisms and evolution of voids still need to be understood in order to further develop current DP steels and postpone failure.

In dual phase steels, it is thought that damage initiates due to local strain and stress concentrations during deformation. These concentrations occur in certain locations; within martensite islands, between ferrite and martensite phases, around inclusions and at ferrite grain boundaries. In the literature, there is no certain guideline on the order or importance of different damage mechanisms. This is mainly due to the complex interaction between phases as well as variation in the mechanical properties of ferrite and martensite [8–12]. On the other hand, it is clear that, damage evolution in dual phase steels occurs in three stages; void initiation, growth and coalescence [13–15].

Experimental research on damage mechanisms can be classified into two main groups; in-situ and post-mortem analyzes. In-situ methods have the advantage of correlating sequential images and gathering

* Corresponding author.
E-mail address: e.e.asik@utwente.nl (E.E. Aşık).

https://doi.org/10.1016/j.msea.2018.10.018
Received 12 July 2018; Received in revised form 2 October 2018; Accepted 4 October 2018
Available online 13 October 2018
0921-5093/

history dependent information often only from the surface. Developments in X-ray micro-tomography may annihilate this restriction of in-situ methods by providing 3D information [16]. Post-mortem methods, on the other hand, give a better understanding on what has happened under the surface. In the work of Taşan et al. [17], in-situ analyzes combined with scanning electron microscopy (SEM) was used to investigate void nucleation in the thick central martensite band and local strain distribution between ferrite and martensite. It was shown that void nucleation sites and high strain bands were coinciding. Maire et al. [16] used X-ray micro-tomography and quantified void initiation and evolution in a volume under increasing strain. This study gives valuable insight on the distribution of voids along different directions (longitudinal, transverse).

Alternatively, post-mortem analyses are frequently used for damage characterization by many researchers [18–22]. Avramovic-Cingara et al. [19], investigated two different DP600 steels. They observed martensite cracking, and ferrite-martensite decohesion. In addition, they qualitatively commented on the high number of voids at the center martensite band. On the other hand, Kadkhodapour et al. [12] studied damage mechanisms in a commercial DP800 steel and they observed mainly ferrite-ferrite interface damage. Lai et al. [22] worked on dual phase steels with different martensite fractions. They found that the martensite fraction had an effect on the dominating damage mechanism. At high martensite fractions cracking of martensite was the main mechanism, whereas at low martensite fractions interface decohesion was more important.

In the present work, we use post-mortem analyzes and scanning electron microscopy to investigate active damage mechanisms and evolution of voids in a DP600 sheet. For this purpose, interrupted tensile tests were conducted both in rolling (RD) and transverse directions (TD). Damage mechanisms were characterized in terms of void nucleation sites, while damage evolution was quantified in terms of % damaged area, number of damage incidents, average nearest neighbor distance, and void distribution. In order to differentiate between void nucleation and growth characteristics, voids were categorized depending on their size. Finally, similarities and differences were compared for RD and TD.

2. Experimental details

2.1. General characteristics of DP600 sheet

The material used in this study is a commercial cold-rolled and annealed DP600 steel sheet with a thickness of 1.20 mm. Composition of the alloying elements is given in Table 1. The material has a dual phase microstructure, which consists of ferrite matrix and martensite islands. Additionally, negligible amount of (less than 0.1 vol%) cementite and retained austenite are present. Initial microstructure of the steel sheet is shown in Fig. 1. Martensite phase exhibits a random distribution when observed from sheet normal, Fig. 1(a). However, micrographs taken from rolling and transverse directions clearly show the banded microstructure that is present in DP600 sheet, Fig. 1(b,c). This type of microstructural inhomogeneity is very common in steel sheets. Banded distribution of the phases is attributed to segregation of substitutional alloying elements during solidification at the interdentritic spaces. Subsequent deformation causes elongated and parallel bands of high- and low-solute rich regions, which later on influences the transformation temperatures [23,24].

Table 1
Chemical compositions (wt%) of the alloying elements in DP600 sheet.

C	Cr	Mn	Si	P, S
0.09	0.5	1.9	0.06	Trace

2.2. Interrupted tensile tests

Interrupted tensile test samples had a standard dog-bone geometry with a gauge length equal to 75 mm and a width equal to 12.5 mm as described in ASTM-E8 [25]. Additionally, thickness of the samples were directly equal to the sheet thickness, 1.2 mm. Samples were prepared along the rolling (RD) and transverse (TD) directions from the DP600 sheet. Interrupted tensile tests were conducted at room temperature with a 100 kN capacity screw driven electromechanical test system (Zwick Testing Machines Ltd, UK). During the tests, a cross-head speed of 5 mm/min, which corresponds to a strain rate equal to 0.001 s^{-1}, was kept constant. The average longitudinal strain was recorded with a non-contact laser speckle extensometer (Messphysik Materials Testing GMBH, Austria) over a relatively large gauge length of 40 mm. This length was intentionally selected in order to minimize the possibility of necking close to the strain measurement points. Three reference tensile tests were conducted, in both directions, until failure during which the strain field was determined by digital image correlation system (Aramis, GOM GmbH, Germany). In the calculations, a facet size was selected 15 × 15 px and the distance between two facets was 13 px.

Table 2 shows some of the crucial mechanical properties of the sheet in RD and TD. The values are calculated by averaging 5 measurements found from the interrupted tensile tests in which the interruption point is further than necking strain. It can be seen that the standard deviation of the properties is rather small. For that reason, a single sample was tested for each interruption point, which makes 14 samples in total. 7 interruption points were chosen to stop the tests. 2 of these were before the necking point, i.e. between 10% and 18% engineering strain. For the remaining 5 interruption points, different levels of load drop, in percentage with respect to the UTS, were used. These levels were chosen as 1%, 3.5%, 5%, 7.5%, and 10%, which cover a wide range to observe the evolution of damage. Fig. 2 shows the engineering stress-strain curves for the steel sheet. The interruption points are shown with markers on the curves to make them clear. It can be seen that until necking, the deformation response in both directions are very similar, however, failure occurs faster in transverse direction.

In the literature, this type of study is mostly carried out on a cross-section of a failed specimen and then the evolution is later correlated from the thickness change of the tensile test sample [19,26,22]. However, this approach has 2 basic disadvantages. Firstly, strain localization at the neck reaches to values around 50–60% before fracture and it decreases with a very high gradient back to values around 15%. As a result, the possible measurement areas confine to very small regions. This can be seen from the results of digital image correlation (DIC) measurement in Fig. 3 which shows true longitudinal strain at the center-line (across width) of samples just before failure as a function of distance from the localized region (neck). Although the local longitudinal strain in TD sample was higher than in RD sample the opposite is seen on the average strain measurement. Secondly, these studies associate relative thickness reduction with the longitudinal strain which is a questionable assumption. This is due to the fact that in order to use thickness reduction, one measures the average thickness strain which, due to texture anisotropy the strain in the width direction, might evolve differently.

Fig. 4 compares two different methods of calculating longitudinal strain at the neck. The strain denoted on the x-axis is approximated by matching the stress level of each specimen at the interruption point to that of 3 reference DIC measurements. This leads to an approximation of the strain value with a level of uncertainty. However, it can be seen that except one of the points, the deviation is small. The uncertainty occurs due to the very small slope of the load-displacement curve. The y-axis, on the other hand, is estimated by assuming no volume change during deformation and calculated from the width of the thinnest part and from the thickness of the imaging area of the actual specimens. The figure shows that after necking the calculated strain underestimates the values inside the neck. This is mainly due to effect of strain

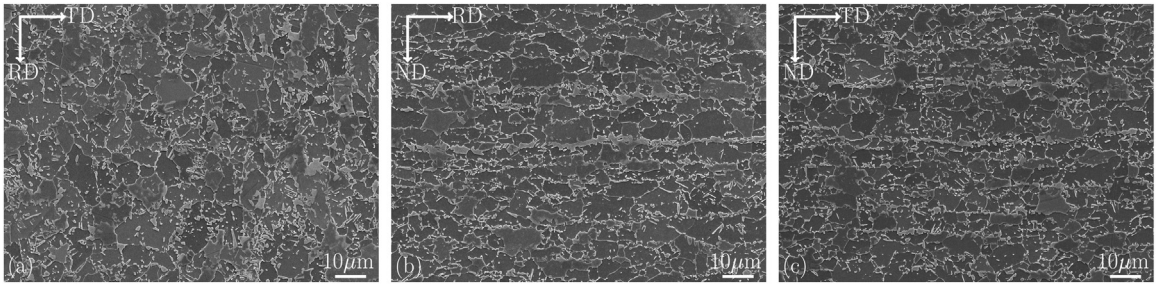

Fig. 1. Initial microstructure of the DP600 sheets looking from (a) normal, (b) transverse and (c) rolling directions. Dark gray matrix is ferrite and the lighter colored islands are martensite.

Table 2
Mechanical Properties of the DP600 sheet in rolling (RD) and transverse directions (TD).

	Yield Strength (MPa)	UltimateTensile Strength (MPa)	UniformTensile Strain(%)
RD	400 ± 9	660 ± 6	18 ± 0.15
TD	412 ± 6	659 ± 2	17 ± 0.36

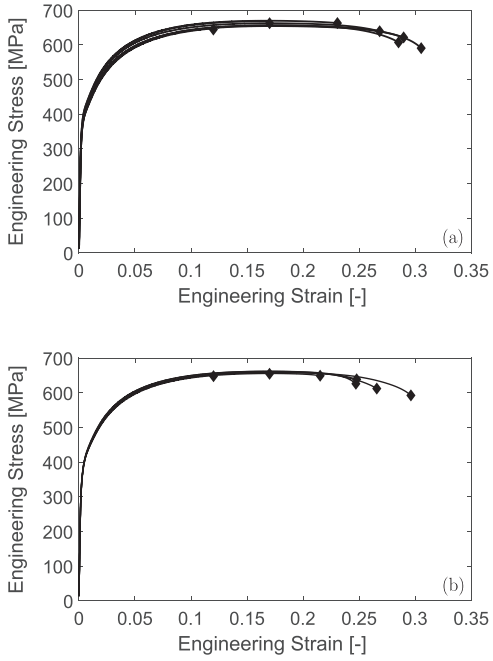

Fig. 2. Engineering stress strain response of DP600 sheet loaded along a) rolling and b)transverse directions. Interruption points showed with round markers.

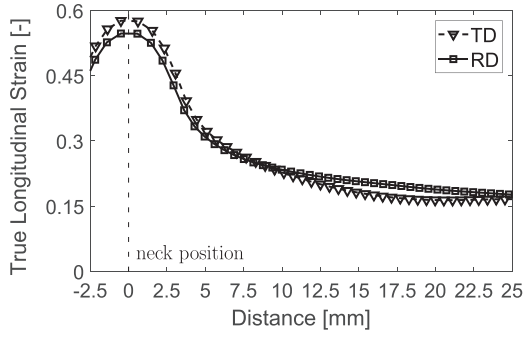

Fig. 3. True longitudinal strain distribution along reference sample. Dashed line indicates position of localization.

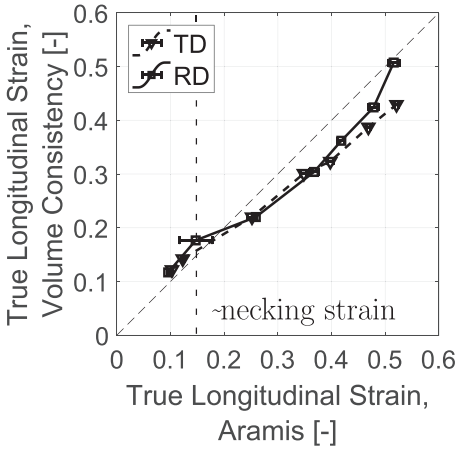

Fig. 4. Comparison of calculated strain from average values with respect to the measured strain by Aramis.

concentration at the center of samples. Based on this observation, the Aramis measurement is deemed to be more reliable and therefore used as the main strain reporting measure in this work.

2.3. Metallographic investigations

A field emission scanning electron microscope (Jeol-SEM 7200F Ltd, Japan) was used for imaging microstructures. The images were recorded with a resolution of 2560 × 2048 pixels. In addition, the microscope was equipped with 2 EDX detectors (Oxford Instruments plc, UK) for elemental analysis.

Metallographic cross-sections, along the loading direction, were prepared from the localized part of the interrupted tensile test samples. For the samples without localization, a random central section was used. The section, denoted A-A section, in Fig. 5 shows a schematic representation of the region of interest (ROI). Samples were cut by an abrasive cutter and subsequently, embedded into Bakelite. Afterwards, metallographic samples were ground down to 4000 grit SiC paper followed by polishing in the range of 3–0.25 μm diamond suspensions. Specimens were immersed into 4% Nital solution for 7 s in order to have sufficient contrast between ferrite and martensite.

2.4. Image processing

Void evolution was quantified by using the polished cross-sectional micrographs. The images were captured at 250x magnification, which corresponds to an area equal to 0.18 mm^2. This magnification scale satisfies a resolution high enough to identify voids as well as an area large enough to observe general characteristics of void properties such as size, number, and distribution. In order to quantify the voids, a 4-step MATLAB© algorithm was developed, as shown in Fig. 6.

The algorithm is based on binarizing the image after identifying

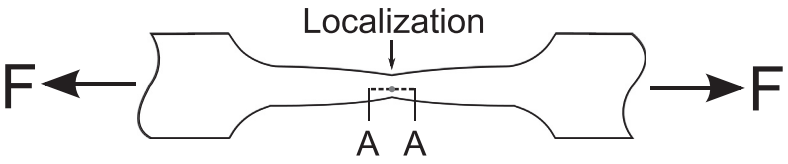

Fig. 5. Schematic top-view of the sample after interrupted tensile test. The section denoted by A-A shows the position and the orientation of the metallographic samples.

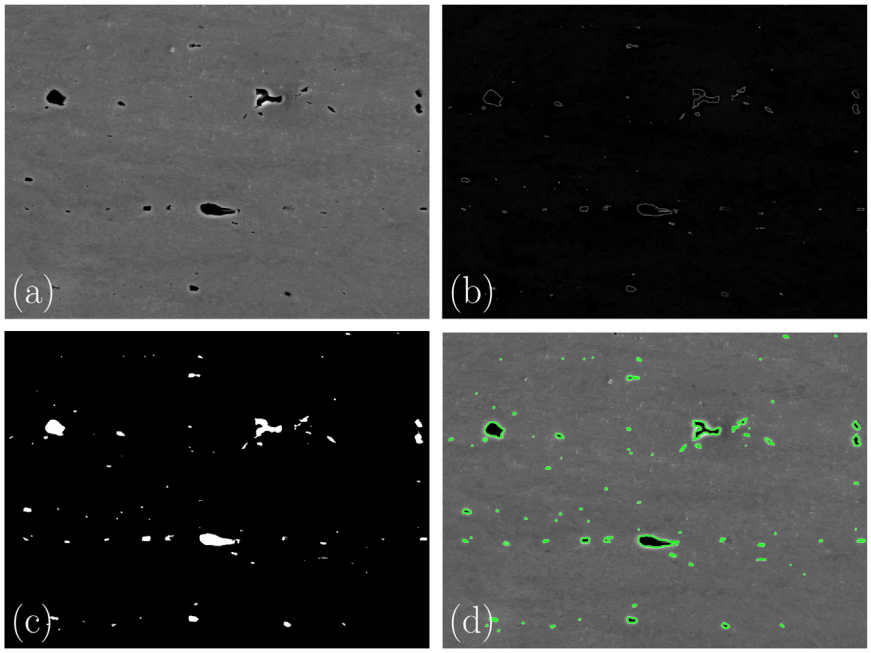

Fig. 6. Automated image processing. (a) original image, (b) edges image, (c) black and white image and (d) analyzed voids circulated in green.

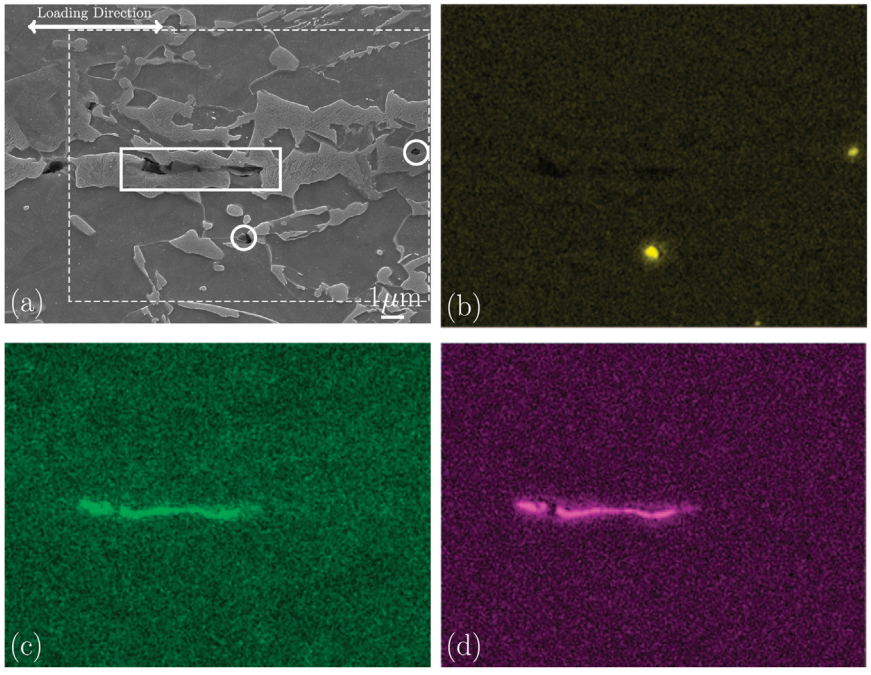

Fig. 7. Voids nucleated due to inclusions. (a) Secondary electron image showing; the scanning area for elemental distributions as the white dashed box and with white circles and white solid box the Al and MnS inclusions. EDX map scanning images for Al (b), Mn (c) and S (d).

void edges. Firstly, the background noise was removed by subtracting the original image from the blurred image. Image blurring was applied using a large (100 px) Gaussian filter. Secondly, a compound edge image was calculated by combining two different edge detection methods. The first edge image was calculated by using the gradient of the pixel values in x and y directions. The second one was obtained by using Kirsch compass kernels in all eight directions [27]. The combination of these two creates an image that is sharper and has well defined edges. In the third step, the edge image was transformed into a binary, black and white, representation. Thanks to the high contrast

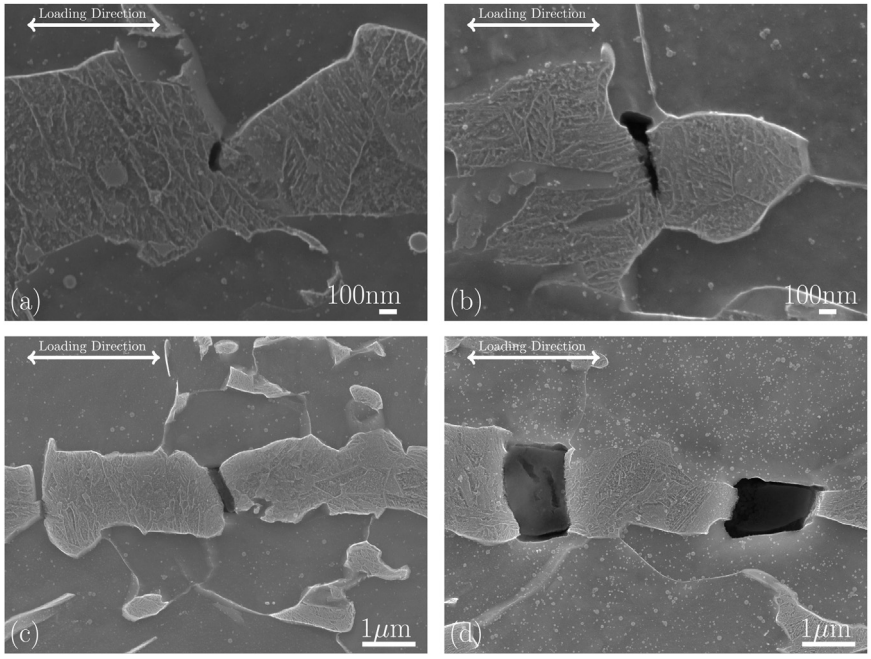

Fig. 8. Voids formed by cracking of martensite. Arrow shows the loading direction (a), (b) sample stretched in TD and (c), (d) sample stretched in RD.

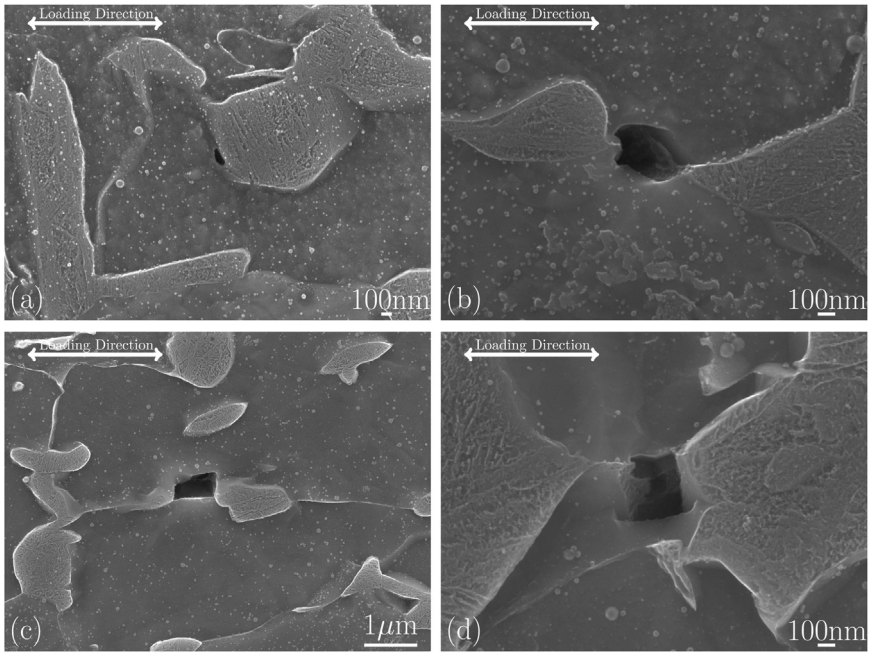

Fig. 9. Voids formed by interface decohesion between ferrite and martensite phases. Arrow shows the loading direction (a), (b) sample stretched in TD and (c), (d) sample stretched in RD.

obtained by the edge detection step, a standard automated threshold detection is sufficient for this transformation. It is important here to note that by using the aforementioned steps, one can fully automatize image processing and minimize human interaction which will result in more standardized and unbiased results. Finally, edges of voids were indexed by using *bwboundaries* function that is found in the standard image processing toolbox of MATLAB© by setting a critical size of 4 pixels (0.14 μm).

3. Results and discussions

3.1. Damage mechanisms

This section approaches damage in a qualitative manner. The main aim is to understand and characterize active damage mechanisms in DP steels leading to failure. In the literature, three damage mechanisms, i.e. void nucleation sites, are commonly reported for ferritic-martensitic dual phase steels [8,9,12,19,22,28]. These mechanisms are classified according to their relationship with the surroundings. In this section, observed damage mechanisms and their general characteristics are discussed.

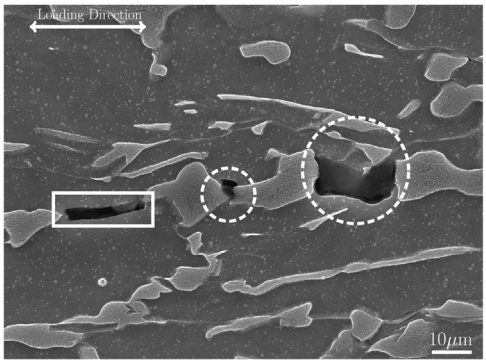

Fig. 10. Aligned voids along loading direction. White solid square shows and interface damage between martensite and ferrite. white dashed cirlces show voids formed by cracking of martensite.

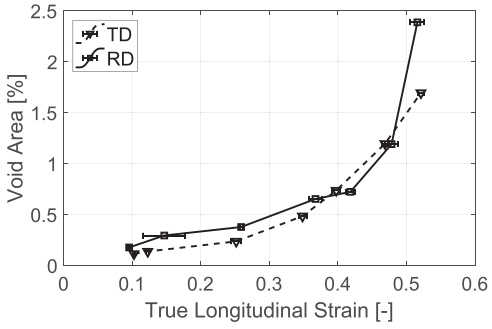

Fig. 11. Void evolution in terms of % area.

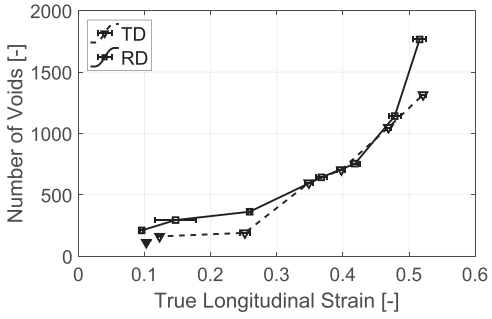

Fig. 12. Number of voids in 0.18 mm^2.

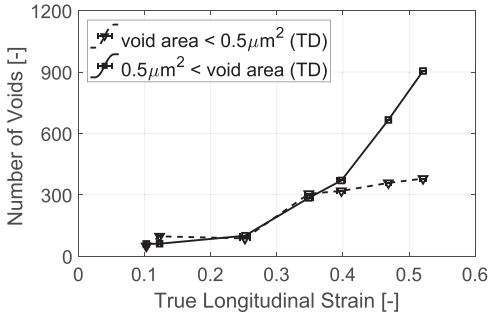

Fig. 13. Void nucleation vs void growth in samples loaded in transverse direction.

The first of the observed damage mechanism is void formation due to inclusions. In steel sheets, inclusions are inevitable and present inclusions causes early void formation. Despite the fact that with modern production techniques, the number of inclusions is limited, completely avoiding them is still not possible. Fig. 7 shows a rare event where

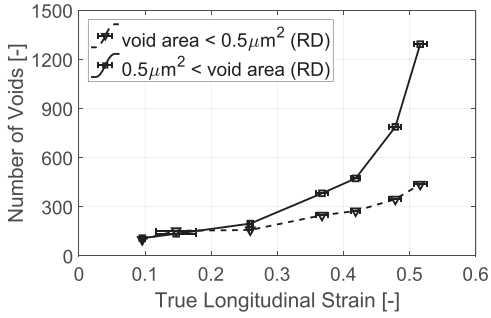

Fig. 14. Void nucleation vs void growth in samples loaded in rolling direction.

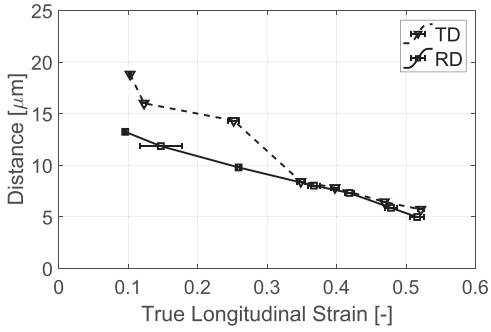

Fig. 15. Change of the average nearest neighbor distance.

Fig. 7(a) is the secondary electron image, with the arrow indicating loading direction and the white solid box and two white circles showing damage due to non-metallic inclusions. This shows that during the early stages of deformation inclusions can cause void formation by decohesion. In this case also MnS inclusions crack due to their rod-like shape. Further information on this type of damage can be found in [29,30].

The second mechanism for void formation is martensite cracking which was the most common mechanism observed in this study. Fig. 8 shows some example cases both for samples along TD and RD. Initially, a crack nucleates at one side of the martensite as in Fig. 8(a,b). Subsequent deformation propagates the crack perpendicular to loading direction, Fig. 8(c). In the end, crack reaches the other end of martensite island and voids starts growing in the loading direction due to deformation of surrounding ferrite Fig. 8(d). This process results in elongated voids with the thickness of the martensite island, that it belonged to.

The last mechanism for void formation is decohesion between martensite and ferrite. In Fig. 9 demonstrative examples of damage occurring at the interface are presented. A general characteristic of interface damage is that void growth occurs in the direction of plastic flow. However, in the early stages of void growth, grain boundaries and orientation of ferrite plays an important role. As can be seen from Fig. 9(c), a void does not grow elliptically in the loading direction, instead, it has sharp corners in the ferrite grain. Moreover, it does not equally grow into the neighboring ferrite grain.

As deformation proceeds, damage incident density increases. Consequently, voids formed by different mechanisms can be observed together in a small area. Fig. 10 shows three voids formed by martensite cracking and ferrite-martensite decohesion mechanisms. As a common observation, these voids also exhibit a banded structure as observed in the distribution of martensite. Later on, these aligned voids may coalesce easily by the 'necklace' mechanism [31,32].

To summarize, for the DP600 steel used in the present study, the main mechanism leading to failure is coalescence of voids that are caused by martensite cracking. During deformation, martensite cracks from weak spots and forms voids. This leads to a decrease in the load carrying capability of the microstructure, causing extensive localized

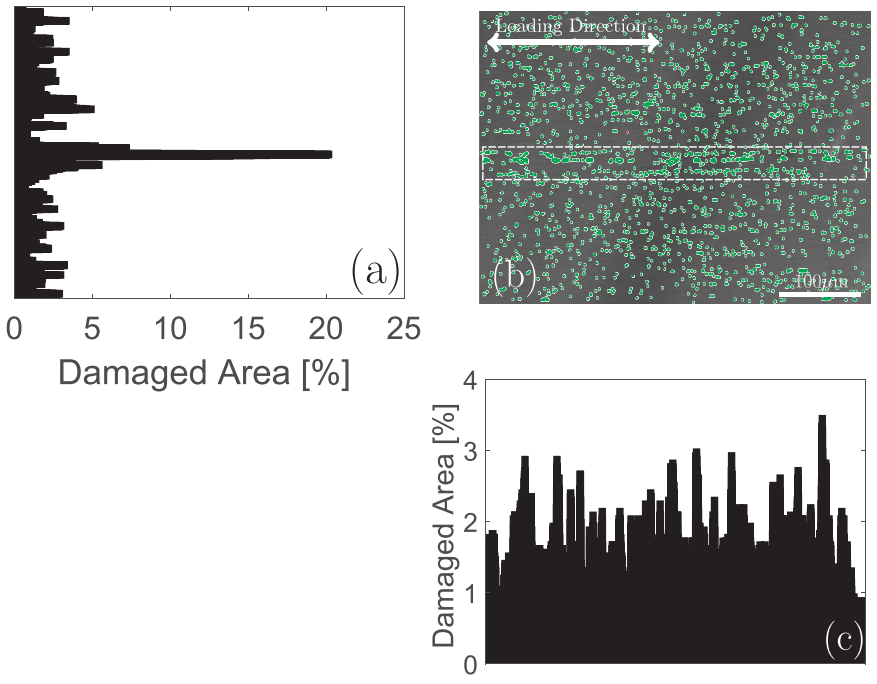

Fig. 16. Void distribution in RD sample, a)void distribution along the thickness direction, b)identified voids, c)void distribution along the loading direction. The white boxed indicate regions where voids are distributed along a band.

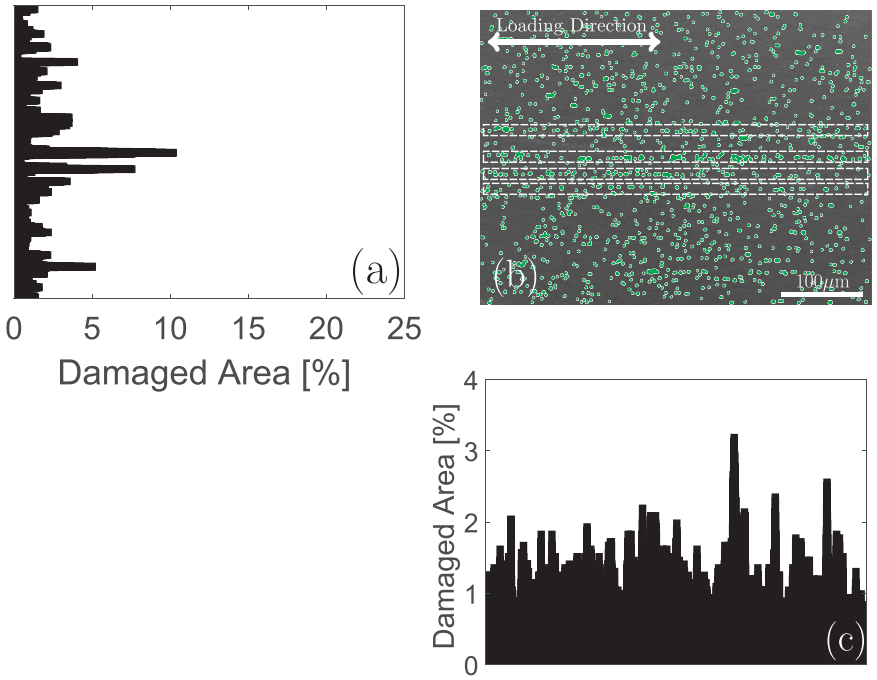

Fig. 17. Void distribution in TD sample, a)void distribution along thickness direction, b)identified voids, c)void distribution along loading direction. The white boxed indicate regions where voids are distributed along a band.

deformation of ferrite surrounding the voids. In the meantime, voids form at the interfaces due to the mismatch between plastic deformation of martensite and ferrite. As deformation continues, more and more voids form by these two mechanisms and ferrite grains keep deforming till formed voids coalesce, resulting in failure. In addition to these phenomena, during deformation of ferrite grains, void nucleation with in the ferrite phase was not observed.

3.2. Damage evolution

In this section, a quantitative approach is followed in order to understand the damage evolution during straining of DP600 sheet. The main focus points are the change in % void area, the number of voids and the average nearest neighbor distance.

Fig. 11 shows the increase of total damaged area with respect to increasing strain. As a first observation, it is noted that void formation occurs before macroscopic localization, i.e. diffuse necking starts, which takes place at approximately 15% strain. Secondly, damage

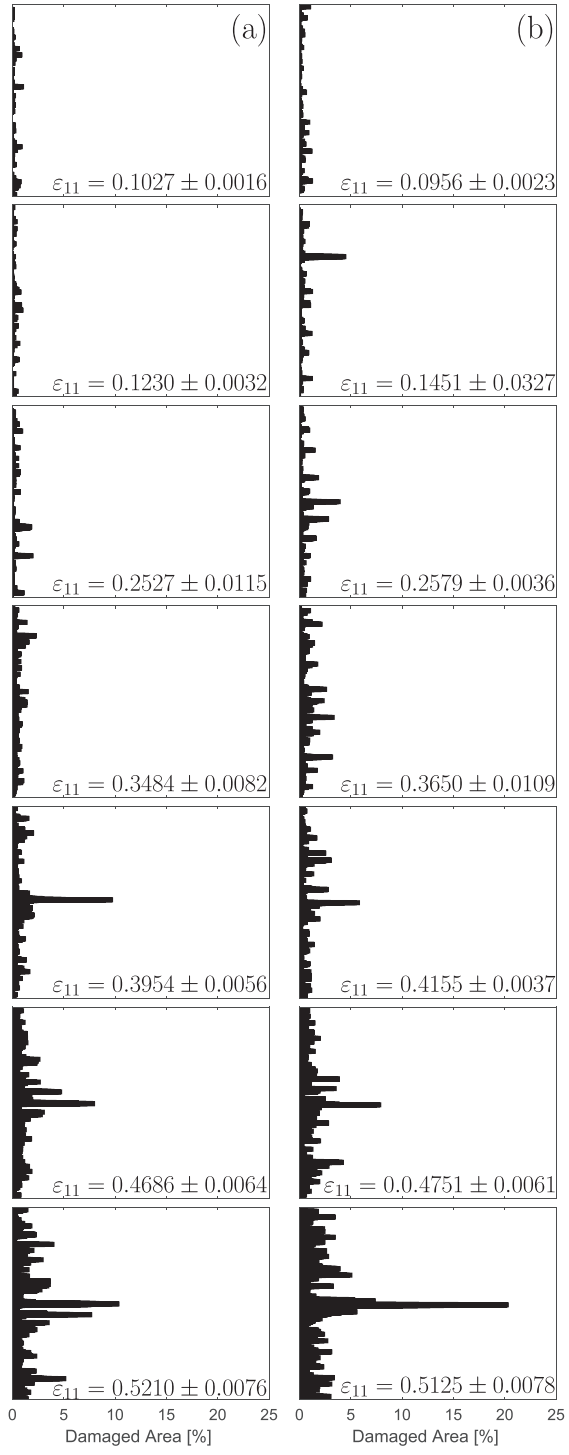

Fig. 18. Void distribution along thickness direction, a)TD, b)RD samples.

evolution occurs slower and almost linearly up to a certain level of strain. This level is around 42% for RD and it is significantly lower, at around 26%, for TD. Further deformation results in an exponential increase of void area.

Fig. 12 shows the evolution of in terms of the number of voids. It is observed that the number of damage instances evolve similarly to the damaged area fraction. However, the level of strain at which the number of voids starts increasing exponentially in RD is lower compared to the level in areal evolution. This suggests a higher void nucleation rate than growth rate for RD samples in that region.

In order to distinguish void nucleation and growth, voids are categorized depending on their areal size, in Fig. 13 and 14. Damage incidents smaller than 0.5 μm^2 are classified as freshly nucleated voids, whereas bigger incidents are classified as grown voids. The characteristic behavior is that with increasing strain, number of voids which are bigger (grown) and smaller (freshly nucleated) than the critical size increase. This suggests that during deformation both void nucleation and void growth take place. However, rate of increase in the voids bigger than the critical size is faster. In the samples loaded along the TD, at a strain range between 0.25% and 0.35%, a step wise increase in the number of nucleated voids is observed. On the other hand, along RD direction that behavior is not present. This might be due to the morphology difference of the martensite phase.

Fig. 15 shows the decrease in average nearest neighbor distance, which essentially shows the closeness of two voids. This factor has a direct relation to the coalescence of voids. During deformation it is observed that the nearest neighbor distance decreases in a linear fashion in RD, whereas in TD, it first decreases down to a certain point with an increasing rate after which it slows down. The final distance is smaller in the RD sample which is also linked to the larger number of voids in RD.

To summarize, in both straining directions, voids are observed before the macroscopic necking of the samples. With further deformation both the number and the total area of the voids increase. The rate of void nucleation and growth initially is rather small, however, it increases rapidly. Moreover, inter-void spacing decreases in a linear fashion which is be related to nucleation of new voids, growth of existing voids as well as decrease in the thickness of the specimens.

3.3. Void distribution

In this section, the damage in the samples are investigated in terms of the distribution of the damaged area across the thickness with respect to the loading direction. Fig. 16 and 17 show the identified voids and their spatial distribution in the most strained specimens. The graphs on the left of the secondary electron images show distribution of voids along the thickness, whereas the graphs under the images represent the void distribution along the loading direction. It is observed that along the loading direction the distribution of the damaged area is quite homogeneous whereas along the thickness direction a clear concentration around the mid-plane stands out. Furthermore, the size of the peak is larger in RD compared to that of TD.

Fig. 18 shows the evolution of the spatial void distribution along the thickness with an increasing strain in samples loaded in the TD (left column) and the RD (right column). At the initial interruption points, void distribution evolves homogeneously for both of the loading directions. Subsequent deformation causes high concentration of voids at the center, where thicker martensite bands are observed. In samples loaded along the rolling direction, the concentration occurred at a centrally located single band, whereas in those loaded along the transverse direction, multiple bands are observed along the thickness of the specimen, as seen in the last row of 18. It is also possible to make a similar observation by comparing identified voids in the white boxes of Fig. 16 and 17. This might be caused by the difference in martensite band continuity. In RD, the central martensite band is longer and more continuous than TD due to rolling operations. One deviation from the general behavior is the 2nd interruption of sample loaded along RD where the high peak was caused by a inclusion related damage incident.

4. Conclusions

In this research, the focus was on investigating the active damage mechanisms in a commercial DP steel grade, both qualitatively and quantitatively, with special emphasis on the anisotropic nature of evolution of voids. To this end, tensile tests were carried out in TD and RD and the voids were observed using a combination of DIC and proposed image analysis steps which provide reproducible and objective

quantification. Three active damage mechanisms, in terms of where voids nucleate, were identified, in line with literature. These are nucleation at inclusions, martensite cracking and decohesion at the ferrite-martensite interface. It is also observed that voids nucleate before UTS is reached.

The evolution of damage is characterized by interrupted tests where the damaged area and the number of voids are tracked separately. A strong correlation between these two quantities is found. One level deeper however, it can be observed that the nucleation rate is slower than the growth rate.

The spatial distribution of voids is investigated and it is found that the average nearest neighbor distance decreases, as expected, with increasing strain. However, the rate at which this occurs is found to be dependent also on the loading direction.

Finally, it is found that the void evolution across the thickness direction is not uniform due to the banded nature of the martensite phase. The morphology of the band is direction dependent and since the main void nucleation mechanism is found to be martensite cracking, this leads to an anisotropy with respect to the loading direction. In the stronger banded direction, along RD, voids are found to nucleate more inhomogeneously.

Data availability

The raw/processed data required to reproduce these findings cannot be shared at this time as the data also forms part of an ongoing study.

Acknowledgments

The authors would like to thank Tata Steel R&D, IJmuiden in the Netherlands for providing the material of this study and Dr. Eisso Atzema for his insightful comments and discussions. This research was carried out under project number F61.1.13486 in the framework of the Partnership Program of the Materials innovation institute M2i (www.m2i.nl) and the Foundation of Fundamental Research on Matter (FOM) (http://www.fom.nl) which is part of the Netherlands Organization for Scientific Research (http://www.nwo.nl).

References

[1] M. Rashid, Dual phase steels, Annu. Rev. Mater. Res. 11 (1981) 245–266.
[2] W. Bleck, Cold-rolled, high-strength sheet steels for auto applications, JOM 48 (7) (1996) 26–30.
[3] R. Kuziak, R. Kawalla, S. Waengler, Advanced high strength steels for automotive industry, Arch. Civil. Mech. Eng. 8 (2) (2008) 103–117, https://doi.org/10.1016/S1644-9665(12)60197-6.
[4] R. Davies, Influence of martensite composition and content on the properties of dual phase steels, Metall. Trans. A 9 (5) (1978) 671–679.
[5] A.-P. Pierman, O. Bouaziz, T. Pardoen, P. Jacques, L. Brassart, The influence of microstructure and composition on the plastic behaviour of dual-phase steels, Acta Mater. 73 (2014) 298–311, https://doi.org/10.1016/j.actamat.2014.04.015.
[6] H. Ghassemi-Armaki, R. Maaß, S. Bhat, S. Sriram, J. Greer, K. Kumar, Deformation response of ferrite and martensite in a dual-phase steel, Acta Mater. 62 (2014) 197–211, https://doi.org/10.1016/j.actamat.2013.10.001.
[7] C. Tasan, M. Diehl, D. Yan, M. Bechtold, F. Roters, L. Schemmann, C. Zheng, N. Peranio, D. Ponge, M. Koyama, K. Tsuzaki, D. Raabe, An overview of dual-phase steels: advances in microstructure-oriented processing and micromechanically guided design, Annu. Rev. Mater. Res. 45 (1) (2015) 391–431.
[8] J.P.M. Hoefnagels, C.C. Tasan, F. Maresca, F.J. Peters, V.G. Kouznetsova, Retardation of plastic instability via damage-enabled microstrain delocalization, J. Mater. Sci. 50 (21) (2015) 6882–6897.
[9] C. Tasan, J. Hoefnagels, M. Diehl, D. Yan, F. Roters, D. Raabe, Strain localization and damage in dual phase steels investigated by coupled in-situ deformation experiments and crystal plasticity simulations, Int. J. Plast. 63 (2014) 198–210, https://doi.org/10.1016/j.ijplas.2014.06.004 (deformation Tensors in Material Modeling in Honor of Prof. Otto T. Bruhns.).
[10] J. Kang, Y. Ososkov, J.D. Embury, D.S. Wilkinson, Digital image correlation studies for microscopic strain distribution and damage in dual phase steels, Scr. Mater. 56 (11) (2007) 999–1002, https://doi.org/10.1016/j.scriptamat.2007.01.031.
[11] M. Mazinani, W. Poole, Effect of martensite plasticity on the deformation behavior of a low-carbon dual-phase steel, Metall. Mater. Trans. A 38 (2) (2007) 328–339.
[12] J. Kadkhodapour, A. Butz, S.Z. Rad, Mechanisms of void formation during tensile testing in a commercial, dual-phase steel, Acta Mater. 59 (7) (2011) 2575–2588.
[13] Y. Su, J. Gurland, Strain partition, uniform elongation and fracture strain in dual-phase steels, Mater. Sci. Eng. 95 (1987) 151–165, https://doi.org/10.1016/0025-5416(87)90507-6.
[14] A. Fillafer, C. Krempaszky, E. Werner, On strain partitioning and micro-damage behavior of dual-phase steels, Mater. Sci. Eng.: A 614 (2014) 180–192, https://doi.org/10.1016/j.msea.2014.07.029.
[15] H. Toda, A. Takijiri, M. Azuma, S. Yabu, K. Hayashi, D. Seo, M. Kobayashi, K. Hirayama, A. Takeuchi, K. Uesugi, Damage micromechanisms in dual-phase steel investigated with combined phase- and absorption-contrast tomography, Acta Mater. 126 (2017) 401–412, https://doi.org/10.1016/j.actamat.2017.01.010.
[16] E. Maire, O. Bouaziz, M.D. Michiel, C. Verdu, Initiation and growth of damage in a dual-phase steel observed by x-ray microtomography, Acta Mater. 56 (18) (2008) 4954–4964.
[17] Micro-mechanical Characterization of Ductile Damage in Sheet Metal (Ph.D. thesis,), Technische Universiteit Eindhoven, 2010.
[18] D.L. Steinbrunner, D. Matlock, G. Krauss, Void formation during tensile testing of dual phase steels, Metall. Trans. A 19 (3) (1988) 579–589.
[19] G. Avramovic-Cingara, Y. Ososkov, M. Jain, D. Wilkinson, Effect of martensite distribution on damage behaviour in dp600 dual phase steels, Mater. Sci. Eng.: A 516 (1–2) (2009) 7–16.
[20] M. Calcagnotto, Y. Adachi, D. Ponge, D. Raabe, Deformation and fracture mechanisms in fine- and ultrafine-grained ferrite/martensite dual-phase steels and the effect of aging, Acta Mater. 59 (2) (2011) 658–670.
[21] H. Ghadbeigi, C. Pinna, S. Celotto, Failure mechanisms in dp600 steel: initiation, evolution and fracture, Mater. Sci. Eng.: A 588 (2013) 420–431, https://doi.org/10.1016/j.msea.2013.09.048.
[22] Q. Lai, O. Bouaziz, M. Gouné, L. Brassart, M. Verdier, G. Parry, A. Perlade, Y. Bréchet, T. Pardoen, Damage and fracture of dual-phase steels: influence of martensite volume fraction, Mater. Sci. Eng.: A 646 (2015) 322–331, https://doi.org/10.1016/j.msea.2015.08.073.
[23] J.D. Verhoeven, A review of microsegregation induced banding phenomena in steels, J. Mater. Eng. Perform. 9 (3) (2000) 286–296, https://doi.org/10.1361/105994900770345935.
[24] R.A. Grange, Effect of microstructural banding in steel, Metall. Trans. 2 (2) (1971) 417–426, https://doi.org/10.1007/BF02663328.
[25] A. Standard, E8, standard test methods for tension testing of metallic materials, Annual Book of ASTM Standards 3 (2004) 57–72.
[26] K. Park, M. Nishiyama, N. Nakada, T. Tsuchiyama, S. Takaki, Effect of the martensite distribution on the strain hardening and ductile fracture behaviors in dual-phase steel, Mater. Sci. Eng.: A 604 (2014) 135–141, https://doi.org/10.1016/j.msea.2014.02.058.
[27] R.A. Kirsch, Computer determination of the constituent structure of biological images, Comput. Biomed. Res. 4 (3) (1971) 315–328, https://doi.org/10.1016/0010-4809(71)90034-6.
[28] H. Ghadbeigi, C. Pinna, S. Celotto, J. Yates, Local plastic strain evolution in a high strength dual-phase steel, Mater. Sci. Eng.: A 527 (18) (2010) 5026–5032, https://doi.org/10.1016/j.msea.2010.04.052.
[29] T.J. Baker, K.B. Gave, J.A. Charles, Inclusion deformation and toughness anisotropy in hot-rolled steels, Met. Technol. 3 (1) (1976) 183–193, https://doi.org/10.1179/030716976803391656.
[30] S.-K. Han, H. Margolin, Void formation, void growth and tensile fracture of plain carbon steel and a dual-phase steel, Mater. Sci. Eng.: A 112 (1989) 133–141, https://doi.org/10.1016/0921-5093(89)90352-3.
[31] A.A. Benzerga, J. Leblond, Ductile fracture by void growth to coalescence, Adv. Appl. Mech. 44 (2010) 169–305.
[32] Q. Lai, O. Bouaziz, M. Gouné, L. Brassart, M. Verdier, G. Parry, A. Perlade, Y. Bréchet, T. Pardoen, Damage and fracture of dual-phase steels: influence of martensite volume fraction, Mater. Sci. Eng.: A 646 (2015) 322–331, https://doi.org/10.1016/j.msea.2015.08.073.